INORGANIC CHEMISTRY FRONTIERS

RESEARCH ARTICLE

View Article Online
View Journal | View Issue

Check for updates

Cite this: *Inorg. Chem. Front.*, 2025, **12**, 4613

Lattice interconversion of 1D ferrocene-based perovskite induced by solvent molecules for selective photocatalytic toluene oxidation†

Yan-Li Yang,‡[a] Ke-Ke Guo,‡[a,b] Xue Bai,[a] An-Ge Zhang,[a] Ying Lu,[a] Mao-Chun Zhu[a] and Shu-Xia Liu *[a]

Metal halide perovskites (MHPs) have attracted enormous attention for potential applications in the fields of optoelectronics and photocatalysis due to their excellent optoelectronic characteristics, such as broad light absorption range, high charge mobility and long carrier diffusion length. However, using MHPs as photocatalysts for photocatalytic toluene oxidation is rare, and the underlying mechanisms affecting toluene oxidation are still unclear. In this study, we constructed two novel one dimensional (1D) ferrocene-based perovskite catalysts, $(C_{13}H_{17}FeNH)PbI_3$ and $(C_{13}H_{17}FeNH)PbI_3$·DEF, of which $(C_{13}H_{17}FeNH)PbI_3$ can photocatalyze the oxidation of toluene to benzaldehyde effectively. It is interesting that the crystal lattices of $(C_{13}H_{17}FeNH)PbI_3$ and $(C_{13}H_{17}FeNH)PbI_3$·DEF can be converted to each other through the gain and loss of solvent molecules, which not only regulates the electronic band structure but also increases the separation efficiency of the photogenerated carriers. These results were confirmed by steady-state photoluminescence (PL) and time-resolved photoluminescence (TRPL) spectra, transient photocurrent response measurements and density functional theory (DFT) calculations. In addition, the lower exciton binding energy (43.2 meV) of $(C_{13}H_{17}FeNH)PbI_3$ further demonstrated its effective carrier separation efficiency. Furthermore, the selective adsorption of $(C_{13}H_{17}FeNH)PbI_3$ on toluene and benzaldehyde provided a prerequisite for the efficient selective oxidation of toluene. Finally, $(C_{13}H_{17}FeNH)PbI_3$ exhibited excellent catalytic activity for the photocatalytic oxidation of toluene to benzaldehyde with a conversion of 28.5% and selectivity (95.3%) towards benzaldehyde.

Received 15th January 2025,
Accepted 31st March 2025

DOI: 10.1039/d5qi00148j

rsc.li/frontiers-inorganic

Published on 02 Agda Baxis 2025. Downloaded on 31/05/2026 10:11:58 PM.

Introduction

Selective oxidation of toluene to benzaldehyde for the production of highly value-added chemicals is important in the chemical industry.[1–4] Benzaldehyde, as an aromatic carbonyl product, is a versatile stepping stone in the manufacturing of perfumes, solvents, dyes, plasticizers, flame retardants, and pharmaceuticals.[5–9] However, to activate the thermodynamically strong and kinetically inert C(sp^3)–H bonds, thermochemical processes are most frequently employed with the use of expensive metal catalysts or hazardous oxidants under harsh reaction conditions (high temperature and/or high pressure).[10,11] Such processes significantly suffer from the difficulty of controlling product selectivity and the simultaneous emission of large amount of waste, making their operation costly, energy-intensive, and environmentally unfriendly. Recently, the photocatalytic oxidation of hydrocarbons using clean and inexhaustible solar energy has garnered wide attention.[12–16] It is well known that the active radicals (*e.g.*, $^{\bullet}O_2^-$ and $^{\bullet}OH$) generated by photocatalysis are extremely reactive with a high redox ability, which enables some challenging reactions to take place under green and mild conditions.[17] Thus, several photocatalytic systems for the activation of C(sp^3)–H bonds under solar or visible light illumination have been reported.

Over the past decade, metal halide perovskites (MHPs) have caused interdisciplinary interest and revolutionized optoelectronic fields due to their outstanding properties, such as excellent light absorption capability, large charge mobility, long carrier diffusion length, and low-cost solution processing.[18–23] Inspired by these merits, in recent years, the utilization of MHPs for solar-to-chemical energy conversion has also received widespread attention, especially in the field

[a]*Key Laboratory of Polyoxometalate and Reticular Material Chemistry of Ministry of Education, Faculty of Chemistry, Northeast Normal University, Changchun, Jilin 130024, P. R. China. E-mail: liusx@nenu.edu.cn*
[b]*Key Laboratory of Eco-Functional Polymer Materials of the Ministry of Education, College of Chemistry and Chemical Engineering, Northwest Normal University, Lanzhou, Gansu 730070, P.R. China*

†Electronic supplementary information (ESI) available. CCDC 2379877 for $(C_{13}H_{17}FeNH)PbI_3$ and 2416757 for $(C_{13}H_{17}FeNH)PbI_3$·DEF. For ESI and crystallographic data in CIF or other electronic format see DOI: https://doi.org/10.1039/d5qi00148j

‡These authors contributed equally to this work.

Published on 02 Agda Baxis 2025. Downloaded on 31/05/2026 10:11:58 PM.

of photocatalysis.[24–27] More importantly, MHPs exhibit excellent catalytic performance as photocatalysts since they have high extinction coefficients, narrow band gaps with highly negative conduction band minimums (CBMs), low exciton binding energies (E_b), and fast charge transport.[28,29] In recent years, some MHPs have become emerging catalysts for the photocatalytic oxidation of toluene. For instance, in 2020, Xu *et al.* employed $A_3Sb_2Br_9$ perovskite nanoparticles (NPs) as a new photocatalyst in the visible-light driven photocatalytic oxidation of toluene, indicating that the photocatalytic activity is strongly related to the distortion of the [$SbBr_6$] octahedron affected by A-site cations.[30] In 2023, Chen *et al.* reported a layered all-inorganic lead-free MHP, $Cs_4ZnSb_2Cl_{12}$, which exhibits excellent photocatalytic performance in the transformation of toluene into benzaldehyde with a conversion rate of 1893 μmol g^{-1} h^{-1} and 95% selectivity.[31] Although some progress has been made in the photocatalytic oxidation of toluene by MHPs, the underlying mechanisms affecting toluene oxidation are still unclear. In addition, lattice changes in MHPs may affect their semiconductor properties, such as photogenerated carrier dynamics, thereby affecting their photocatalytic activity. However, due to the lack of suitable systems, exploring the effect of lattice changes of MHPs on photocatalytic toluene oxidation has not been reported and remains a huge challenge.

In this work, we designed and synthesized two novel one dimensional (1D) ferrocene-based perovskites, ($C_{13}H_{17}FeNH$)PbI_3 and ($C_{13}H_{17}FeNH$)PbI_3·DEF, of which ($C_{13}H_{17}FeNH$)PbI_3 can selectively and effectively photocatalyze the oxidation of toluene to benzaldehyde. Of note, the crystal lattices of ($C_{13}H_{17}FeNH$)PbI_3 and ($C_{13}H_{17}FeNH$)PbI_3·DEF can be converted to each other through the gain and loss of DEF molecules, which not only regulates the electronic band structure, but also increases the separation efficiency of photogenerated carriers. These results were confirmed by steady-state photoluminescence (PL) and time-resolved photoluminescence (TRPL) spectra, transient photocurrent response measurements and density functional theory (DFT) calculations. In addition, the E_b of ($C_{13}H_{17}FeNH$)PbI_3 was calculated to be 43.2 meV, much lower than that of ($C_{13}H_{17}FeNH$)PbI_3·DEF (76.8 meV), further suggesting the effective carrier separation efficiency of ($C_{13}H_{17}FeNH$)PbI_3. Furthermore, the selective adsorption of ($C_{13}H_{17}FeNH$)PbI_3 on toluene and benzaldehyde provides a prerequisite for the efficient selective oxidation of toluene. Finally, ($C_{13}H_{17}FeNH$)PbI_3 exhibited excellent catalytic activity for the photocatalytic oxidation of toluene to benzaldehyde with a conversion of 28.5% and selectivity (95.3%) towards benzaldehyde.

Results and discussion

Crystal structural analysis of ($C_{13}H_{17}FeNH$)PbI_3 and ($C_{13}H_{17}FeNH$)PbI_3·DEF

Although ($C_{13}H_{17}FeNH$)PbI_3 and ($C_{13}H_{17}FeNH$)PbI_3·DEF exhibit similar topological structures, their synthetic methods are vastly different. The *N*,*N*-dimethylaminomethylferrocene-based 1D perovskite single crystal with DEF solvents, ($C_{13}H_{17}FeNH$)PbI_3·DEF, was grown by a conventional solvent evaporation method, while ($C_{13}H_{17}FeNH$)PbI_3 was obtained using an anti-solvent process. Single-crystal X-ray diffraction analysis indicated that ($C_{13}H_{17}FeNH$)PbI_3 crystallizes in the monoclinic $P112_1$ space group, featuring a 1D chain-based three-dimensional (3D) supramolecular structure. As shown in Fig. S1,† the basic structural motif of ($C_{13}H_{17}FeNH$)PbI_3 is composed of one [PbI_3]$^-$ and one protonated *N*,*N*-dimethylaminomethylferrocene ($C_{13}H_{17}FeNH$). Adjacent [PbI_3]$^-$ groups are connected together through coordination bonds between I^- ions and Pb^{2+} ions, forming a 1D anionic chain (Fig. 1a). $C_{13}H_{17}FeNH$ is arranged neatly around this chain as a counter cation to balance the charge. Finally, one 1D chain-based 3D supramolecular structure, ($C_{13}H_{17}FeNH$) PbI_3, is obtained through supramolecular interactions between adjacent 1D chains (Fig. 1b). Of note, as shown in Fig. 1b, the distance of adjacent 1D anionic chains at the (002) crystal planes is 13.2 Å. Interestingly, the C–N bond of $C_{13}H_{17}FeNH$ can rotate around the C atom as the center (Fig. 1c), which provides a prerequisite for the lattice change of ($C_{13}H_{17}FeNH$)PbI_3.

As shown in Fig. 1d, DEF is embedded into the lattice of ($C_{13}H_{17}FeNH$)PbI_3·DEF in the form of molecules through hydrogen bonding interactions (Fig. S2†), which affects the rearrangement of $C_{13}H_{17}FeNH$ in the lattice, resulting in the number of layers of $C_{13}H_{17}FeNH$ in the lattice of these two perovskites changing from a single layer of ($C_{13}H_{17}FeNH$)PbI_3 to double layers of ($C_{13}H_{17}FeNH$)PbI_3·DEF. This leads to a longer distance between the adjacent 1D anionic chains at the (002) crystal planes (17.3 Å) of ($C_{13}H_{17}FeNH$)PbI_3·DEF compared to ($C_{13}H_{17}FeNH$)PbI_3. This lattice change induced by solvent molecules may cause differences in the semiconductor properties of these two perovskites, thereby affecting the photocatalytic activity. Pertinent crystal data and relevant refinement parameters for ($C_{13}H_{17}FeNH$)PbI_3 and ($C_{13}H_{17}FeNH$)PbI_3·DEF are listed in Table S1.†

Lattice interconversion of ($C_{13}H_{17}FeNH$)PbI_3 and ($C_{13}H_{17}FeNH$)PbI_3·DEF

Firstly, powder X-ray diffraction (PXRD) was performed to confirm the successful synthesis of ($C_{13}H_{17}FeNH$)PbI_3 and ($C_{13}H_{17}FeNH$)PbI_3·DEF. As shown in Fig. 2a, the PXRD patterns of the synthesized ($C_{13}H_{17}FeNH$)PbI_3 and ($C_{13}H_{17}FeNH$) PbI_3·DEF match well with their simulated ones from the simulated single crystal data, illustrating their good phase purities. It should be noted that the diffraction peak position of the (002) crystal plane of ($C_{13}H_{17}FeNH$)PbI_3 (7.2°) is obviously greater than that ($C_{13}H_{17}FeNH$)PbI_3·DEF (5.3°), which further indicates that the lattice of ($C_{13}H_{17}FeNH$)PbI_3·DEF is larger than that of ($C_{13}H_{17}FeNH$)PbI_3, consistent with their crystallographic data. The (002) crystal planes of the two perovskites represented in the crystal structure can be found in Fig. S3.† Due to the weak interaction between the DEF molecule and $C_{13}H_{17}FeNH$ in the lattice of ($C_{13}H_{17}FeNH$)PbI_3·DEF, we found that ($C_{13}H_{17}FeNH$)PbI_3 and ($C_{13}H_{17}FeNH$)PbI_3·DEF can be con-

 This journal is © the Partner Organisations 2025

Published on 02 Agda Baxis 2025. Downloaded on 31/05/2026 10:11:58 PM.

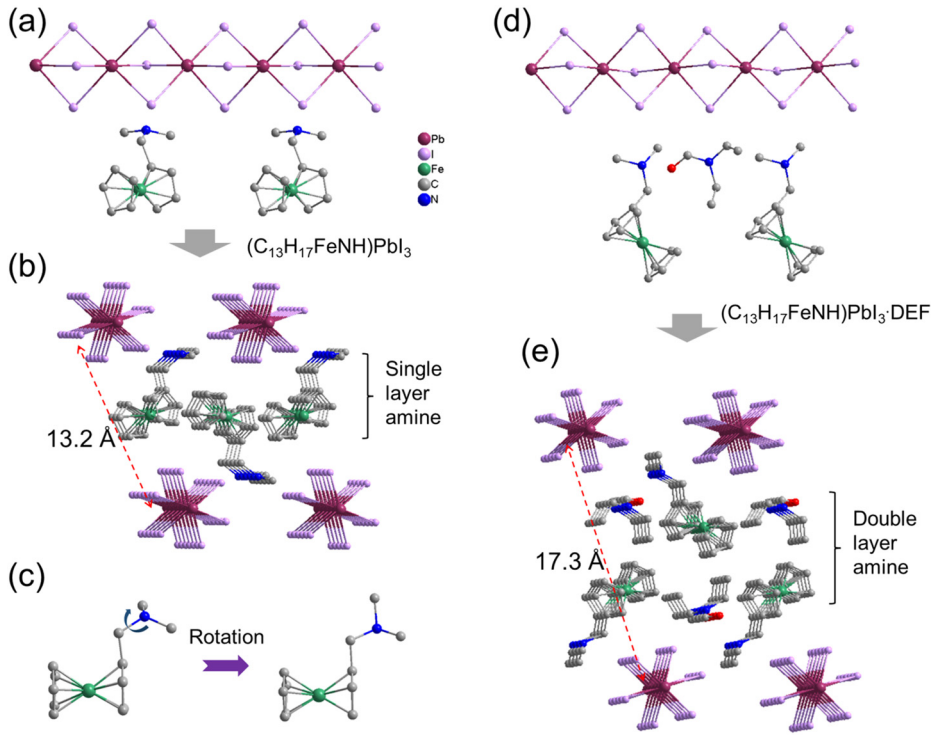

Fig. 1 1D chain structure of $(C_{13}H_{17}FeNH)PbI_3$ (a); 1D chain-based 3D supramolecular structure of $(C_{13}H_{17}FeNH)PbI_3$ (b); rotation diagram of the C–N bond of $C_{13}H_{17}FeNH$ (c); 1D chain structure of $(C_{13}H_{17}FeNH)PbI_3$·DEF (d); 3D supramolecular structure of $(C_{13}H_{17}FeNH)PbI_3$·DEF (e).

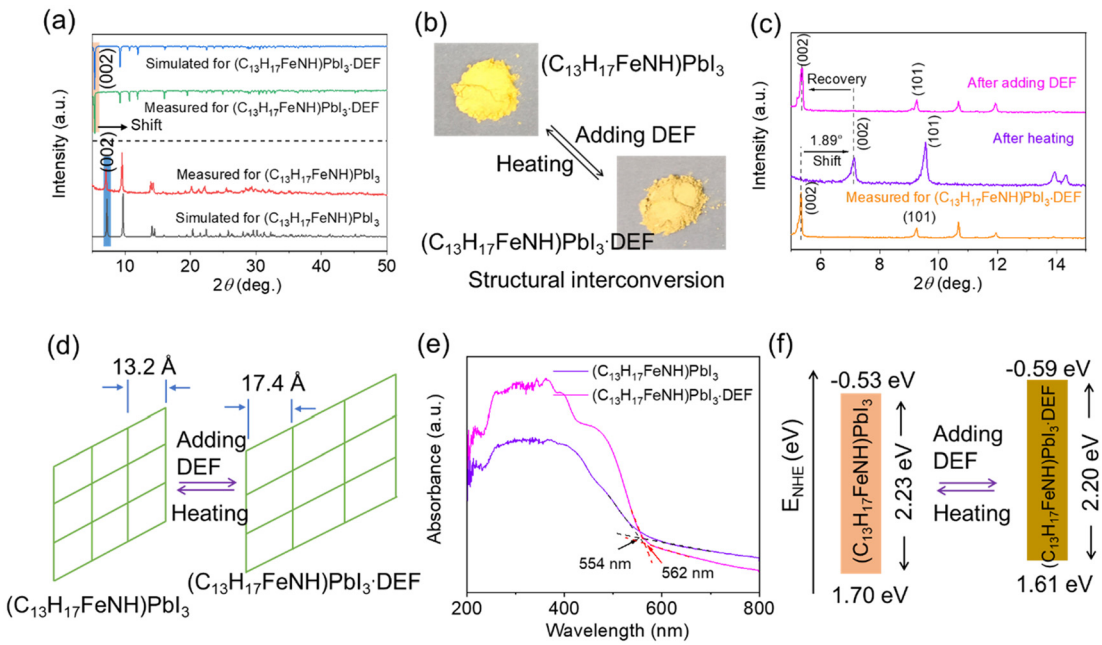

Fig. 2 As-synthesized and simulated PXRD patterns of $(C_{13}H_{17}FeNH)PbI_3$ and $(C_{13}H_{17}FeNH)PbI_3$·DEF single crystal powders (a); photos of $(C_{13}H_{17}FeNH)PbI_3$ and $(C_{13}H_{17}FeNH)PbI_3$·DEF powders and schematic of their structural interconversion (b); PXRD pattern changes of $(C_{13}H_{17}FeNH)PbI_3$·DEF after heating and adding DEF (c); schematic of lattice transformation between $(C_{13}H_{17}FeNH)PbI_3$ and $(C_{13}H_{17}FeNH)PbI_3$·DEF (d); UV-vis diffuse reflectance spectra of $(C_{13}H_{17}FeNH)PbI_3$ and $(C_{13}H_{17}FeNH)PbI_3$·DEF samples (e); electronic band structure diagram of $(C_{13}H_{17}FeNH)PbI_3$ and $(C_{13}H_{17}FeNH)PbI_3$·DEF (f).

Published on 02 Agda Baxis 2025. Downloaded on 31/05/2026 10:11:58 PM.

verted to each other through the gain and loss of solvent molecules. As illustrated in Fig. 2b, $(C_{13}H_{17}FeNH)PbI_3$ can be transformed into $(C_{13}H_{17}FeNH)PbI_3$·DEF by adding DEF dropwise, while, by heating, $(C_{13}H_{17}FeNH)PbI_3$·DEF can be converted into $(C_{13}H_{17}FeNH)PbI_3$ gradually. This structural interconversion was also revealed by changes in the PXRD patterns. As shown in Fig. 2c, when $(C_{13}H_{17}FeNH)PbI_3$·DEF was heated at 80 °C for 20 min, the diffraction peak position of the (002) crystal plane after heating shifted towards a larger angle by 1.89°. It's interesting that the diffraction peak position of the (002) crystal plane after adding DEF returned to the original position of $(C_{13}H_{17}FeNH)PbI_3$·DEF. This also demonstrates that the lattice interconversion between $(C_{13}H_{17}FeNH)PbI_3$ and $(C_{13}H_{17}FeNH)PbI_3$·DEF can be achieved by controlling the gain and loss of solvent molecules. As shown in Fig. 2d, this lattice interconversion may lead to differences in the photoelectric properties of these two perovskites, further affecting their photocatalytic activities. The effect of DEF molecules on the thermal stabilities of these two perovskites was investigated by thermogravimetric analysis (TGA). As show in Fig. S4,† for $(C_{13}H_{17}FeNH)PbI_3$·DEF, the weight loss of about 10.4% at 25–85 °C corresponds to DEF molecules. Then, its framework starts to decompose at approximately 180 °C. $(C_{13}H_{17}FeNH)PbI_3$, due to the lack of DEF molecules in the crystal lattice, does not possess a weight loss process at 25–85 °C and maintains excellent thermal stability until 180 °C.

The electronic band structures of $(C_{13}H_{17}FeNH)PbI_3$ and $(C_{13}H_{17}FeNH)PbI_3$·DEF were then investigated.

The UV-vis diffuse reflectance spectra (DRS) of $(C_{13}H_{17}FeNH)PbI_3$ and $(C_{13}H_{17}FeNH)PbI_3$·DEF powder samples were obtained first to evaluate their bandgaps (E_g) (Fig. 2e). E_g can be defined as the intersection point between the energy axis and the line extrapolated from the linear portion of the adsorption edge in the plot of the Kubelka–Munk function F against E. $F = (1 - R)^2/2R$ was transformed from the measured diffuse reflectance data, in which R presents the reflectance of an infinitely thick layer at a given wavelength.[32,33] As shown in Fig. S5a and b,† the E_g of $(C_{13}H_{17}FeNH)PbI_3$ and $(C_{13}H_{17}FeNH)PbI_3$·DEF were calculated to be 2.23 eV and 2.20 eV, respectively. Then, we calculated the conduction band minima (CBM) of $(C_{13}H_{17}FeNH)PbI_3$ and $(C_{13}H_{17}FeNH)PbI_3$·DEF through Mott-Schottky plots. As illustrated in Fig. S6,† the flat band potential (E_{fb}) of $(C_{13}H_{17}FeNH)PbI_3$ was calculated to be −0.67 eV *vs.* SCE, corresponding to −0.43 eV *vs.* NHE. Considering the CBM could be 0–0.1 eV more negative than the E_{fb}, the CBM of $(C_{13}H_{17}FeNH)PbI_3$ equals −0.53 eV *vs.* NHE.[34] As shown in Fig. S7,† the CBM of $(C_{13}H_{17}FeNH)PbI_3$·DEF was calculated to be −0.59 eV *vs.* NHE. The position of the valence band maxima (VBM) of $(C_{13}H_{17}FeNH)PbI_3$ and $(C_{13}H_{17}FeNH)PbI_3$·DEF were calculated to be 1.70 eV and 1.61 eV, respectively, based on the E_g and CBM. Thus, the electronic band structure diagrams of $(C_{13}H_{17}FeNH)PbI_3$ and $(C_{13}H_{17}FeNH)PbI_3$·DEF are shown in Fig. 2f. Due to the lattice change induced by DEF molecules, the electronic band structures between $(C_{13}H_{17}FeNH)PbI_3$ and $(C_{13}H_{17}FeNH)PbI_3$·DEF can be effectively regulated.

Low exciton binding energy and excellent photoelectrochemical properties

For photocatalysts, the separation efficiency of photogenerated carriers is a key factor affecting the photocatalytic performance. The PL and TRPL spectra were thus investigated. As shown in Fig. 3a, the relatively lower PL emission for $(C_{13}H_{17}FeNH)PbI_3$ compared to that of $(C_{13}H_{17}FeNH)PbI_3$·DEF is due to the recombination of the photogenerated electron-hole being effectively suppressed, indicating low exciton binding energy and favorable charge transport. As shown in Fig. 3b, the TRPL curves of $(C_{13}H_{17}FeNH)PbI_3$ and $(C_{13}H_{17}FeNH)PbI_3$·DEF can be well fitted by a double-exponential function[35]

$$I(t) = A_1 \exp\left(-\frac{t}{\tau_1}\right) + A_2 \exp\left(-\frac{t}{\tau_2}\right) \quad (1)$$

where τ_1 and τ_2 are the decay times of the first and second decay components, respectively, and A_1 and A_2 are the amplitudes of the first and second decay components, respectively. The amplitudes of the decay components reflect the total contribution of each lifetime component toward the average lifetime (τ_{ave}), which can be calculated as follows.[36,37]

$$\tau_{ave} = \frac{A_1\tau_1^2 + A_2\tau_2^2}{A_1\tau_1 + A_2\tau_2} \quad (2)$$

All fitting parameters are tabulated in Table S2,† and τ_{ave} (0.352 ns) of $(C_{13}H_{17}FeNH)PbI_3$ is shorter than that of $(C_{13}H_{17}FeNH)PbI_3$·DEF (0.541 ns), which further illustrates the higher separation efficiency and transfer ability of photogenerated charges of $(C_{13}H_{17}FeNH)PbI_3$. Temperature-dependent photoluminescence was employed to explore the exciton binding energies of both perovskites. Fig. 3c and Fig. S8† show the temperature-dependent PL intensity plots of $(C_{13}H_{17}FeNH)PbI_3$ and $(C_{13}H_{17}FeNH)PbI_3$·DEF, respectively. The PL intensity decreases with the increase of temperature. The exciton binding energy is calculated by fitting the relation curve between PL integral intensity and temperature through the following equation[38,39]

$$\frac{1}{I(T)} = A + B\exp\left(-\frac{E_b}{k_b T}\right) \quad (3)$$

where I is PL intensity, A and B are the fitting parameters, E_b represents exciton binding energy, k_b is the Boltzmann constant, and T is temperature. From Fig. 3d, the E_b of $(C_{13}H_{17}FeNH)PbI_3$ was calculated to be 43.2 meV, which is much lower than that of $(C_{13}H_{17}FeNH)PbI_3$·DEF (76.8 meV), further indicating the greater separation efficiency of photogenerated carriers of $(C_{13}H_{17}FeNH)PbI_3$. Transient photocurrent response measurements can directly reflect the separation efficiency of photogenerated carriers. As shown in Fig. 3e, the photocurrent density of $(C_{13}H_{17}FeNH)PbI_3$ can reach as high as 9.1 μA cm^{-2}, about 3.3 times more than that of $(C_{13}H_{17}FeNH)PbI_3$·DEF (2.7 μA cm^{-2}). The higher photocurrent density of $(C_{13}H_{17}FeNH)PbI_3$ illustrates its higher separation efficiency of photogenerated carriers.

 This journal is © the Partner Organisations 2025

Published on 02 Agda Baxis 2025. Downloaded on 31/05/2026 10:11:58 PM.

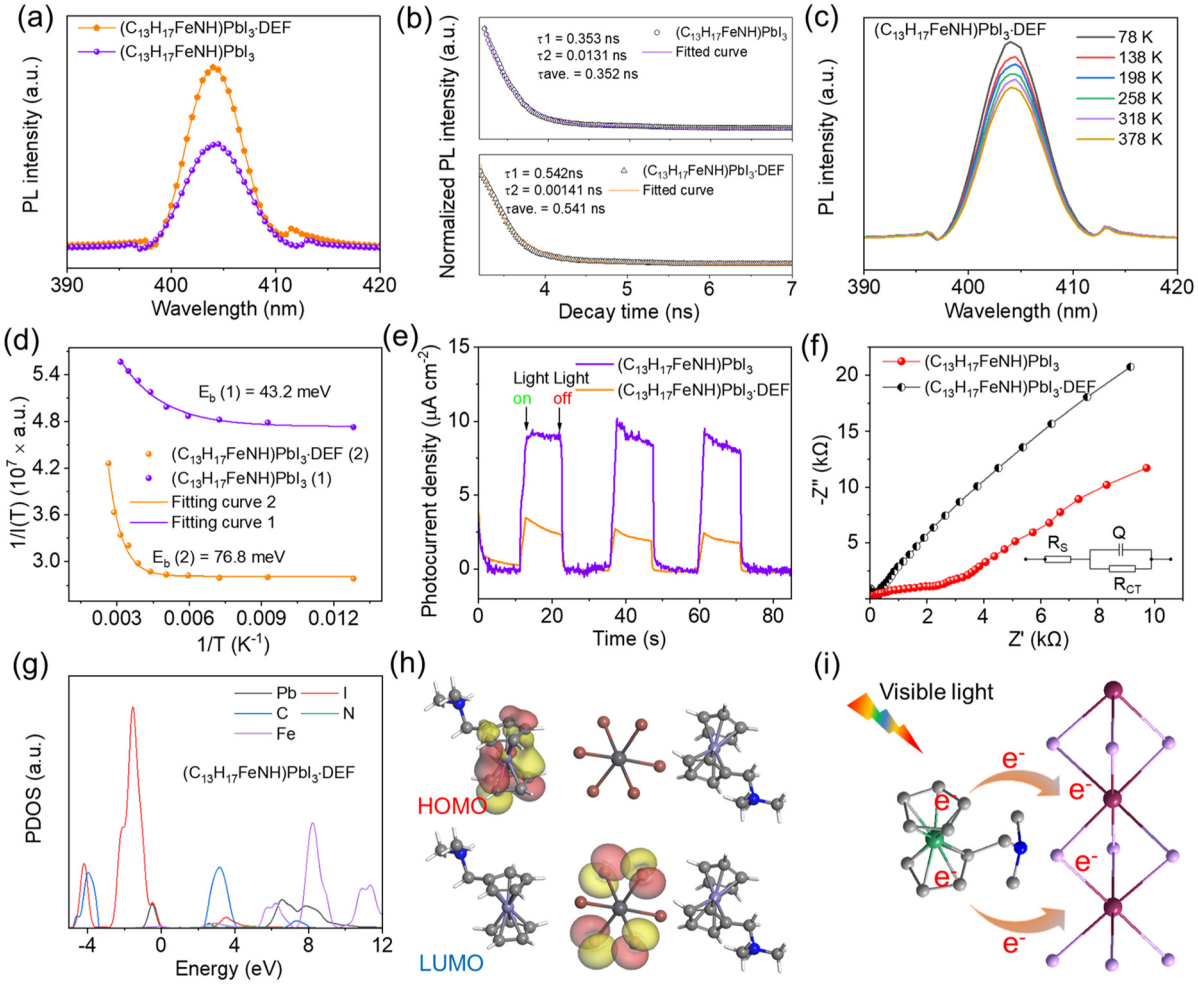

Fig. 3 PL (a) and TRPL (b) spectra of $(C_{13}H_{17}FeNH)PbI_3$ and $(C_{13}H_{17}FeNH)PbI_3$·DEF, respectively; temperature-dependent PL intensity plots of $(C_{13}H_{17}FeNH)PbI_3$ (c); exciton binding energies from fitting the integrated PL intensity to temperature (d); transient photocurrent responses of $(C_{13}H_{17}FeNH)PbI_3$ and $(C_{13}H_{17}FeNH)PbI_3$·DEF under 0.5 V bias voltage (e); electrochemical impedance spectroscopy of $(C_{13}H_{17}FeNH)PbI_3$ and $(C_{13}H_{17}FeNH)PbI_3$·DEF (f); PDOS plots of $(C_{13}H_{17}FeNH)PbI_3$ (g); HOMO and LUMO of $(C_{13}H_{17}FeNH)PbI_3$ (h); schematic of charge transition process of $(C_{13}H_{17}FeNH)PbI_3$ (i).

The electrochemical impedance spectroscopy (EIS) Nyquist plots of $(C_{13}H_{17}FeNH)PbI_3$ and $(C_{13}H_{17}FeNH)PbI_3$·DEF were measured to illustrate their capacities of charge separation and transfer (Fig. 3f). The equivalent circuit diagram is inserted. From fitting the EIS data, the charge transfer resistance values (R_{CT}) of $(C_{13}H_{17}FeNH)PbI_3$ and $(C_{13}H_{17}FeNH)PbI_3$·DEF electrodes were found to be 4.58×10^4 Ω and 7.82×10^4 Ω, respectively. In general, the smaller the R_{CT}, the smaller the radius of the impedance spectrum, which means a higher efficiency of charge separation and transfer. Thus, the charge transfer capacity of $(C_{13}H_{17}FeNH)PbI_3$ is larger than that of $(C_{13}H_{17}FeNH)PbI_3$·DEF. To further reveal the contributions of different atoms of these two perovskites to the LUMO and HOMO orbitals, as well as the differences of the charge transfer process of these two perovskites, DFT calculations were carried out. As shown in Fig. 3g, the electron density of the LUMO orbital of $(C_{13}H_{17}FeNH)PbI_3$ mainly lies on the I 5p and Pb 6s orbitals of the $[PbI_3]^-$ group. The HOMO orbital of $(C_{13}H_{17}FeNH)PbI_3$ is mostly concentrated on the C 2p and Fe 3d orbitals of the $C_{13}H_{17}FeNH$ group. These results show that the electrons of $(C_{13}H_{17}FeNH)PbI_3$ primarily transition from the C 2p and Fe 3d orbitals of $C_{13}H_{17}FeNH$ to the I 5p and Pb 6s orbitals of the $[PbI_3]^-$ group (Fig. 3h and i), indicating the efficient separation of photogenerated carriers. However, in contrast to $(C_{13}H_{17}FeNH)PbI_3$, the HOMO and LLUMO orbitals of $(C_{13}H_{17}FeNH)PbI_3$·DEF are both contributed by the $C_{13}H_{17}FeNH$ groups (Fig. S9†), illustrating that the presence of DEF molecules in the crystal lattice is not conducive to the separation of photogenerated carriers, which is consistent with the PL, TRPL, and transient photocurrent response measurements.

Photocatalytic oxidation of toluene

To explore the influence of lattice changes induced by DEF on photocatalytic activities, the photocatalytic C(sp^3)–H bond activation in toluene molecules was investigated under visible

Published on 02 Agda Baxis 2025. Downloaded on 31/05/2026 10:11:58 PM.

light irradiation (λ > 420 nm) using these two perovskites as catalysts at room temperature (Fig. 4a). As shown in Fig. 4b, both $(C_{13}H_{17}FeNH)PbI_3$ and $(C_{13}H_{17}FeNH)PbI_3$·DEF can photocatalyze the oxidation of toluene, but the yield of benzaldehyde over $(C_{13}H_{17}FeNH)PbI_3$ is higher than the yield using $(C_{13}H_{17}FeNH)PbI_3$·DEF as catalyst within all reaction times. Using $(C_{13}H_{17}FeNH)PbI_3$ as photocatalyst, the amount of benzaldehyde after 4 h of reaction can reach as high as 251 μmol, which is about 1.8 times higher than that of $(C_{13}H_{17}FeNH)PbI_3$·DEF (140 μmol). As shown in Fig. 4c, the selectivity of $(C_{13}H_{17}FeNH)PbI_3$ towards BA is as high as 95.3%, which is larger than that of $(C_{13}H_{17}FeNH)PbI_3$·DEF (73%). In addition, both $(C_{13}H_{17}FeNH)PbI_3$ and $(C_{13}H_{17}FeNH)PbI_3$·DEF have very low selectivity for BY production, with 3.2% and 12%, respectively. Of note, the conversion rate of toluene using $(C_{13}H_{17}FeNH)PbI_3$ as catalyst can reach 28.5%, which is also larger than that of $(C_{13}H_{17}FeNH)PbI_3$·DEF (26%). These results indicate that the DEF molecules in the crystal lattice of $(C_{13}H_{17}FeNH)PbI_3$·DEF are not conducive to its photocatalytic activity for toluene oxidation. We further compared the catalytic performance of $(C_{13}H_{17}FeNH)PbI_3$ with those of some other reported catalysts, as shown in Table S3.† The results indicate that $(C_{13}H_{17}FeNH)PbI_3$ possesses excellent catalytic performance for photocatalytic toluene oxidation. As shown in Fig. 4d, the apparent quantum efficiency (AQE) value for the oxidation of toluene to benzaldehyde on $(C_{13}H_{17}FeNH)PbI_3$·DEF is 2.5%. $(C_{13}H_{17}FeNH)PbI_3$ presents the significantly increased AQE of 4.3%, further demonstrating the excellent photocatalytic performances of $(C_{13}H_{17}FeNH)PbI_3$. Reusability and stability are important figures of merit to evaluate a catalyst. As shown in Fig. 4e, only a slight decrease in the yield of benzaldehyde (from 251 μmol to 223 μmol) was found after five cycling experiments, indicating that the structural framework of $(C_{13}H_{17}FeNH)PbI_3$ is basically stable after five cycles.

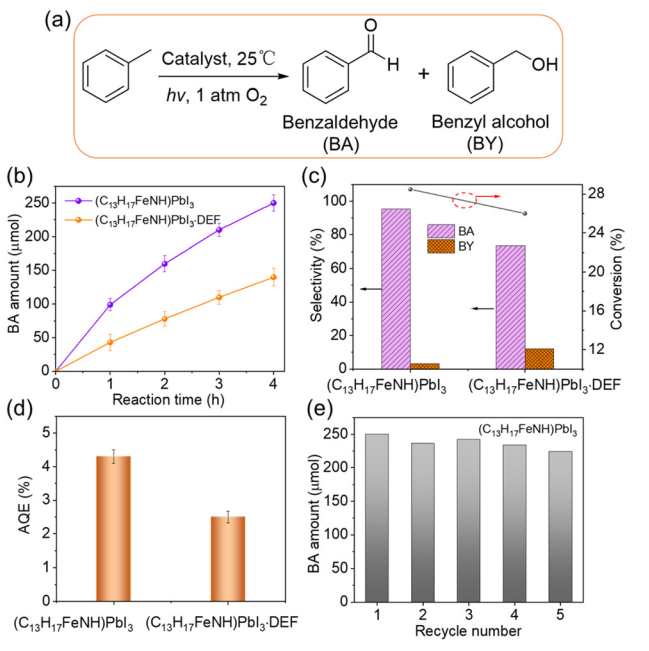

Fig. 4 Photocatalytic selective oxidation of toluene; conditions: photocatalyst (50 mg), toluene (1 mmol), MeCN (3 mL), O_2 (1 atm), λ > 420 nm, and irradiation time (4 h) (a); effect of reaction time on BA amount over $(C_{13}H_{17}FeNH)PbI_3$ and $(C_{13}H_{17}FeNH)PbI_3$·DEF catalysts (b); selectivity of BA and By as well as the conversion of toluene over $(C_{13}H_{17}FeNH)PbI_3$ and $(C_{13}H_{17}FeNH)PbI_3$·DEF catalysts (c); AQE of toluene oxidation for $(C_{13}H_{17}FeNH)PbI_3$ and $(C_{13}H_{17}FeNH)PbI_3$·DEF (λ = 365 nm) (d); photocatalytic cycling experiment for toluene oxidation (e).

For the purpose of further exploring and verifying the catalytic potential of $(C_{13}H_{17}FeNH)PbI_3$, the reactivities of various toluene derivatives were examined under the same conditions (Table 1). When *p*-xylene as a substrate was added into this reaction system, a substrate conversion rate of 37.3% was achieved with a corresponding aldehyde selectivity of 88.4%. In addition, *o*-xylene and *m*-xylene as substrates also present higher conversion than toluene, and the corresponding aldehyde selectivities are around 80%. Several electron-withdrawing *para*-position-substituted toluenes, including –F, –Cl and –Br, were subjected to the optimal conditions, and all can also convert into their corresponding aldehydes. However, compared to toluene, electron-withdrawing substituted toluenes show slightly lower conversion, and electron-donating substituted toluenes show relatively higher conversion. These results indicate that $(C_{13}H_{17}FeNH)PbI_3$ can serve as an effective photocatalyst for photocatalytic oxidation of toluene derivatives.

Photocatalytic mechanism analysis

To clarify the reaction mechanism of photocatalytic toluene oxidation over $(C_{13}H_{17}FeNH)PbI_3$, a series of free-radical-capture experiments were performed to reveal the key reactive species induced by light (Fig. 5a). The introduction of tetramethylpiperidine *N*-oxide (TEMPO) as the quenching agent for all radicals in the reaction completely suppresses the conversion of toluene, indicating the key role of the radicals for toluene oxidation. The addition of *tert*-butanol (TBA) as an $^{\bullet}OH$ scavenger has no noticeable effect on toluene conversion, indicating that $^{\bullet}OH$ is not involved in the reaction. The addition of butylated hydroxytoluene (BHT) as the quenching

Table 1 Substrate scope on $(C_{13}H_{17}FeNH)PbI_3$ [a]

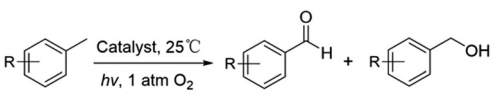

Entry	R	Conv. (%)	Sel.(%) Aldehyde	Alcohol
1	H	28.5	95.3	3.2
2	*o*-CH_3	33.7	81.5	8.7
3	*m*-CH_3	32.1	83.2	9.5
4	*p*-CH_3	37.3	88.4	5.2
5	*p*-F	17.7	82.1	9.4
6	*p*-Cl	21.2	89.6	6.6
7	*p*-Br	24.8	93.0	4.6

[a] Reaction conditions: substrate (1 mmol), MeCN (3 mL), O_2 (1 atm), photocatalyst (50 mg), λ > 420 nm, and reaction time (4 h).

 This journal is © the Partner Organisations 2025

Published on 02 Agda Baxis 2025. Downloaded on 31/05/2026 10:11:58 PM.

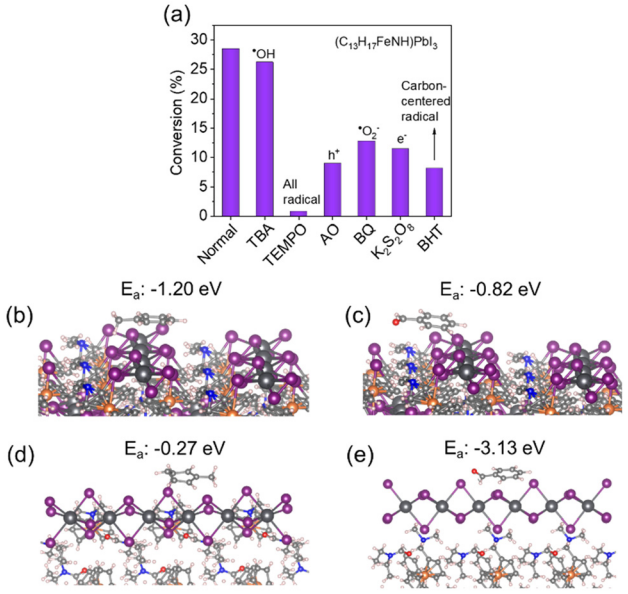

Fig. 5 Control experiments of radical quenching for the photocatalytic oxidation of toluene (a); adsorption models for toluene on $(C_{13}H_{17}FeNH)PbI_3$ (b) and $(C_{13}H_{17}FeNH)PbI_3$·DEF (d); adsorption models for benzaldehyde on (C13H17FeNH)PbI3 (c) and (C13H17FeNH)PbI3·DEF (e).

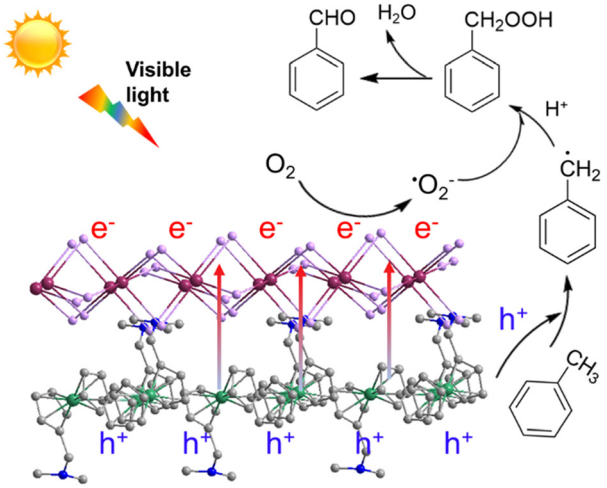

Fig. 6 Possible photocatalytic reaction mechanism of toluene oxidation over $(C_{13}H_{17}FeNH)PbI_3$.

agent of carbon-centered radicals in the reaction produces an apparent decline in toluene conversion, indicating that the carbon-centered radicals are important intermediates for the oxidation of toluene to benzaldehyde. In Fig. 5a, it can be seen that the conversion of toluene was significantly blocked after ammonium oxalate (AO) was added as a hole (h^+) scavenger, suggesting that holes play a key role for toluene conversion. Furthermore, there was a significant decline in toluene conversion when either benzoquinone (BQ) or $K_2S_2O_8$ was added, which are scavengers for superoxide radicals ($^{\bullet}O_2^-$) and photogenerated electrons (e^-), respectively. Since the formation of $^{\bullet}O_2^-$ is through the combination of molecular oxygen with photogenerated electrons, the quenching of photogenerated electrons would result in the decline of $^{\bullet}O_2^-$ formation. The results strongly suggest that the $^{\bullet}O_2^-$ play a critical role in the photocatalytic toluene oxidation.

DFT calculations were further employed to investigate the difference in adsorption capacities of these two perovskites for toluene and benzaldehyde. As shown in Fig. 5b, the calculated adsorption energy (E_{ad}) of toluene molecules on $(C_{13}H_{17}FeNH)PbI_3$ was −1.20 eV, which is substantially lower than that of $(C_{13}H_{17}FeNH)PbI_3$·DEF (−0.27 eV), confirming that the adsorption of toluene on $(C_{13}H_{17}FeNH)PbI_3$ is energy favorable. This is a prerequisite for $(C_{13}H_{17}FeNH)PbI_3$ to exhibit a higher conversion rate to toluene. In addition, considering that a large adsorption energy of the catalyst to the substrate is not conducive to the removal of the substrate from the catalyst, which will affect the selectivity of the catalyst towards the production of substrate, we further calculated the E_{ad} of $(C_{13}H_{17}FeNH)PbI_3$ and $(C_{13}H_{17}FeNH)PbI_3$·DEF for benzaldehyde. As shown in Fig. 5e, the E_{ad} of benzaldehyde on $(C_{13}H_{17}FeNH)PbI_3$·DEF is as low as −3.13 eV, which is much lower than that of $(C_{13}H_{17}FeNH)PbI_3$ (−0.82 eV). This indicates that benzaldehyde is more easily removed from $(C_{13}H_{17}FeNH)PbI_3$, hindering its further oxidation and improving the selectivity of benzaldehyde.

Based on experimental and DFT calculation results, a plausible reaction mechanism for the selective photocatalytic oxidation of toluene to benzaldehyde over $(C_{13}H_{17}FeNH)PbI_3$ can be proposed as follows (Fig. 6): (1) $(C_{13}H_{17}FeNH)PbI_3$ is excited to generate photoinduced electrons and holes under visible light irradiation; (2) the accumulated holes at the VBM of $(C_{13}H_{17}FeNH)PbI_3$ oxidize toluene to yield benzyl radicals and the accumulated electrons at the CBM of $(C_{13}H_{17}FeNH)PbI_3$ react with O_2 to generate $^{\bullet}O_2^-$; (3) benzyl radicals couple with $^{\bullet}O_2^-$ and a proton to form the hydroperoxide intermediate; (4) the hydroperoxide species can be dehydrated to form the benzaldehyde species, which desorbs from $(C_{13}H_{17}FeNH)PbI_3$ quickly due to its low adsorption energy to produce benzaldehyde, avoiding the overoxidation process.

Conclusions

In summary, two novel 1D ferrocene-based perovskites, $(C_{13}H_{17}FeNH)PbI_3$ and $(C_{13}H_{17}FeNH)PbI_3$·DEF, were constructed for the selective photocatalytic oxidation of toluene to benzaldehyde. Impressively, we found that the crystal lattices of $(C_{13}H_{17}FeNH)PbI_3$ and $(C_{13}H_{17}FeNH)PbI_3$·DEF can be converted to each other through the gain and loss of DEF molecules, which not only regulates the electronic band structure, but also increases the separation efficiency of photogenerated carriers. These results were confirmed by PL, TRPL, and transient photocurrent response measurements. In addition, the significantly lower exciton binding energy of $(C_{13}H_{17}FeNH)PbI_3$ further demonstrates its favorable charge separation. Finally, $(C_{13}H_{17}FeNH)PbI_3$ exhibited excellent catalytic activity for the

Published on 02 Agda Baxis 2025. Downloaded on 31/05/2026 10:11:58 PM.

photocatalytic oxidation of toluene to benzaldehyde with a conversion of 28.5% and selectivity (95.3%) towards benzaldehyde. This work reveals the influence of perovskite lattice changes on their optoelectronic properties and photocatalytic performances, which may provide new ideas and insights for designing perovskite-based photocatalysts with highly efficient separation efficiencies of photogenerated carriers and selectivity towards substrates.

Experimental

Materials and characterization

All reagents utilized in this study were of analytical purity and used without additional processing. Additional information regarding the reagents and instrument characterizations can be found in the ESI.†

Synthesis of $C_{13}H_{17}FeNHI$

6.8 mL of HI was dissolved in 15 mL ethyl alcohol, and then 10 mL of $C_{13}H_{17}FeN$ was slowly added dropwise to the above solution. After the mixed solution was stirred in an ice bath for 2 h, $C_{13}H_{17}FeNHI$ powder was obtained using a rotary evaporator and purified by washing with dichloromethane. The $C_{13}H_{17}FeNHI$ powder was dried in a vacuum oven overnight at 55 °C before use.

Synthesis of $(C_{13}H_{17}FeNH)PbI_3$

A mixture of $C_{13}H_{17}FeNHI$ (0.01 mol, 3.71 g) and PbI_2 (0.01 mmol, 4.61 g) was dissolved in 3 mL of DEF in a 10 ml beaker at 50 °C. After stirring at 100 °C for 2 h, the solution was immediately filtered through a 0.45 μm poly(tetrafluoroethylene) filter to obtain a clear perovskite precursor solution. Then, the $(C_{13}H_{17}FeNH)PbI_3$ single crystal can be obtained by placing above solution in a closed container with a dichloromethane atmosphere for 7 days.

Synthesis of $(C_{13}H_{17}FeNH)PbI_3$·DEF

A mixture of $C_{13}H_{17}FeNHI$ (0.01 mol, 3.71 g) and PbI_2 (0.01 mmol, 4.61 g) was dissolved in 3 mL of DEF in a 10 ml beaker at 50 °C. After stirring at 100 °C for 2 h, the solution was immediately filtered through a 0.45 μm poly(tetrafluoroethylene) filter to obtain a clear perovskite precursor solution. Then, the $(C_{13}H_{17}FeNH)PbI_3$·DEF single crystal was obtained after the solution slowly evaporated at 55 °C for 3 days.

Photocatalytic oxidation of toluene experiments

The photocatalytic oxidation of toluene to benzaldehyde was performed in a 10 mL quartz reactor with water-cooling system under visible light irradiation (λ > 420 nm, 100 mW cm^{-2}). A 300 W xenon lamp (Perfect Light Company, Beijing) was chosen as the light source. For each photocatalytic reaction, 1 mmol of toluene, 50 mg of photocatalyst and 3 mL of acetonitrile (CH_3CN) were uniformly mixed in the quartz reactor. O_2 was bubbled through the mixture at a rate of 1.0 mL min^{-1} for 1 h. Then, the quartz reactor was sealed with a balloon to keep the oxygen gas at one atmosphere pressure. The suspension was stirred in the dark for 30 min before illumination. Then, the reaction was carried out under visible light irradiation. After the reaction, the catalyst was removed by centrifugation and the products were directly analyzed with a gas chromatograph (Agilent GC 7820A). The conversion (con.) of toluene and selectivity (sel.) of the products were calculated according to the following equations.[40,41]

$$\text{Con. (\%)} = \frac{\text{moles of toluene reacted}}{\text{moles of initial toluene}} \times 100\% \quad (4)$$

$$\text{Sel. (\%)} = \frac{\text{moles of corresponding product}}{\text{moles of toluene reacted}} \times 100\% \quad (5)$$

Data availability

The data supporting the findings of this study are available from the corresponding authors upon reasonable request.

Conflicts of interest

There are no conflicts to declare.

Acknowledgements

This work is financially supported by the National Natural Science Foundation of China (No. 22071019 and 22172022).

References

1 K. Su, H. Liu, B. Zeng, Z. Zhang, N. Luo, Z. Huang, Z. Gao and F. Wang, Visible-Light-Driven Selective Oxidation of Toluene into Benzaldehyde over Nitrogen-Modified Nb_2O_5 Nanomeshes, *ACS Catal.*, 2019, **10**, 1324–1333.
2 G. Zhou, B. Lei and F. Dong, Lewis Acid Sites in (110) Facet-Exposed BiOBr Promote C–H Activation and Selective Photocatalytic Toluene Oxidation, *ACS Catal.*, 2024, **14**, 4791–4798.
3 S. Wongthep, P. Pluengphon, D. Tantraviwat, W. Panchan, S. Boochakiat, K. Jarusuphakornkul, Q. Wu, J. Chen and B. Inceesungvorn, New visible-light-driven Bi_2MoO_6/$Cs_3Sb_2Br_9$ heterostructure for selective photocatalytic oxidation of toluene to benzaldehyde, *J. Colloid Interface Sci.*, 2024, **655**, 32–42.
4 B. Zhou, K. Fan, Y. Chong, S. Xu, J. Wei, J. Wei, A. A. Sergeev, K. S. Wong, T. Li, G. Chen, D. Ye and K. Yan, Modulating Adsorption–Redox Sites and Charge Separation of $Cs_3Bi_2Br_{9-x}$@AgBr Core–Shell Heterostructure for Selective Toluene Photooxidation, *ACS Energy Lett.*, 2024, **9**, 1743–1752.
5 G. Che, Y. Zhao, W. Yang, Q. Zhou, X. Li, Q. Pan and Z. Su, Preparation of a Nanosheeted Uranyl–Organic Framework

 This journal is © the Partner Organisations 2025

Published on 02 Agda Baxis 2025. Downloaded on 31/05/2026 10:11:58 PM.

for Enhanced Photocatalytic Oxidation of Toluene, *Inorg. Chem.*, 2024, **63**, 10767–10774.

6 H. Li, Y. Meng, C. Shu, X. Li, A. A. Kiss and X. Gao, Innovative Reactive Distillation Process for the Sustainable Synthesis of Natural Benzaldehyde, *ACS Sustainable Chem. Eng.*, 2018, **6**, 14114–14124.

7 H. Huang, H. Fan, Y. Ge, W. Ye, Y. Liu, C. Song, H. Lin, X. Zhang, B. Li, X. Nie, S. Zhang and R. Lu, Solvent-free oxidation of toluene to benzaldehyde using electron-rich Au clusters confined in Silicalite-1, *Chem. Eng. J.*, 2023, **458**, 141446.

8 K.-K. Guo, Y.-L. Yang, S.-M. Dong, F.-Y. Li, X.-Y. Jiang and L. Xu, pH-Controlled assembly of $[ZnW_{12}O_{40}]^{6-}$-based hybrids from a 0D dimer to a 2D network: synthesis, crystal structure, and photocatalytic performance in transformation of toluene into benzaldehyde, *Dalton Trans.*, 2021, **50**, 17308–17318.

9 H. Zhang, S. Liu, A. Zheng, P. Wang, Z. Zheng, Z. Wang, H. Cheng, Y. Dai, B. Huang and Y. Liu, Enhanced Charge Transfer Process and Photocatalytic Activity over a Phosphonate–based MOF via Amorphization Strategy, *Angew. Chem., Int. Ed.*, 2024, **63**, e202400965.

10 J. Long, H. Liu, S. Wu, S. Liao and Y. Li, Selective Oxidation of Saturated Hydrocarbons Using Au–Pd Alloy Nanoparticles Supported on Metal–Organic Frameworks, *ACS Catal.*, 2013, **3**, 647–654.

11 P. Gandeepan and L. Ackermann, Transient Directing Groups for Transformative C–H Activation by Synergistic Metal Catalysis, *Chem*, 2018, **4**, 199–222.

12 B. Yu, S. Zhang and X. Wang, Helical Microporous Nanorods Assembled by Polyoxometalate Clusters for the Photocatalytic Oxidation of Toluene, *Angew. Chem., Int. Ed.*, 2021, **60**, 17404–17409.

13 Y. J. Gao, H. Jin, D. A. Esteban, B. Weng, R. A. Saha, M. Q. Yang, S. Bals, J. A. Steele, H. Huang and M. B. J. Roeffaers, 3D–cavity–confined $CsPbBr_3$ quantum dots for visible–light–driven photocatalytic $C(sp^3)$–H bond activation, *Carbon Energy*, 2024, **6**, e559.

14 Z. Sun, Y. Tan, X. Shi, B. Li, X. Wang, J. Wen, L. Huang and W.-M. Lau, General Method to Introduce π-Electrons into Oxygen-Doped Porous Carbon Nitride for Photocatalytic Hydrogen Evolution and Toluene Oxidation, *ACS Sustainable Chem. Eng.*, 2024, **12**, 1051–1061.

15 H. Wang, C. Cao, D. Li, Y. Ge, R. Chen, R. Song, W. Gao, X. Wang, X. Deng, H. Zhang, B. Ye, Z. Li and C. Li, Achieving High Selectivity in Photocatalytic Oxidation of Toluene on Amorphous BiOCl Nanosheets Coupled with TiO_2, *J. Am. Chem. Soc.*, 2023, **145**, 16852–16861.

16 X. Li, H. Mai, N. Cox, J. Lu, X. Wen, D. Chen and R. A. Caruso, Sb-Substituted $Cs_2AgBiBr_6$/g-C_3N_4 Composite for Photocatalytic $C(sp^3)$–H Bond Activation in Toluene, *Chem. Mater.*, 2023, **35**, 3105–3114.

17 Y. Wang, Y. Du, P. Duan, B. Li, J. Li and Y. Zhu, Asymmetrical facet-oriented anisotropic charge migration of MIL-101(Fe) with internal electric field-steered photogenerated holes for boosting photocatalytic oxidation, *Appl. Catal., B*, 2025, **361**, 124564.

18 T. H. Han, S. Tan, J. Xue, L. Meng, J. W. Lee and Y. Yang, Interface and Defect Engineering for Metal Halide Perovskite Optoelectronic Devices, *Adv. Mater.*, 2019, **31**, 1803515.

19 P. Aggarwal, A. Chaudhary, S. Singh, R. G. Singh and V. G. Rao, Leveraging Phenazine–Based Ligands for Optimized Perovskite Optoelectronic Performance Through Chelation and Redox Engineering, *Adv. Opt. Mater.*, 2024, **13**, 2402047.

20 H. Li, X. Jiang, Q. Wei, Z. Zang, M. Ma, F. Wang, W. Zhou and Z. Ning, Low–Dimensional Inorganic Tin Perovskite Solar Cells Prepared by Templated Growth, *Angew. Chem., Int. Ed.*, 2021, **60**, 16330–16336.

21 S. Zhang, J. Su, J. Zhang, Z. Lin, H. Yuan, J. Chang and Y. Hao, Impacts of the Electron Transport Layer Surface Reconstruction on the Buried Interface in Perovskite Optoelectronic Devices, *J. Phys. Chem. Lett.*, 2021, **12**, 11834–11842.

22 Z. Zhang, Z. Li, Y. Chen, Z. Zhang, K. Fan, S. Chen, L. Liu and S. Chen, Progress on Inkjet Printing Technique for Perovskite Films and Their Optoelectronic and Optical Applications, *ACS Photonics*, 2023, **10**, 3435–3450.

23 C. J. Bartel, J. M. Clary, C. Sutton, D. Vigil-Fowler, B. R. Goldsmith, A. M. Holder and C. B. Musgrave, Inorganic Halide Double Perovskites with Optoelectronic Properties Modulated by Sublattice Mixing, *J. Am. Chem. Soc.*, 2020, **142**, 5135–5145.

24 S. Pan, J. Li, Z. Wen, R. Lu, Q. Zhang, H. Jin, L. Zhang, Y. Chen and S. Wang, Halide Perovskite Materials for Photo (Electro)Chemical Applications: Dimensionality, Heterojunction, and Performance, *Adv. Energy Mater.*, 2021, **12**, 2004002.

25 S. Chen, H. Yin, P. Liu, Y. Wang and H. Zhao, Stabilization and Performance Enhancement Strategies for Halide Perovskite Photocatalysts, *Adv. Mater.*, 2022, **35**, 2203836.

26 J. S. Zhao, Y. F. Mu, L. Y. Wu, Z. M. Luo, L. Velasco, M. Sauvan, D. Moonshiram, J. W. Wang, M. Zhang and T. B. Lu, Directed Electron Delivery from a Pb–Free Halide Perovskite to a Co(II) Molecular Catalyst Boosts CO_2 Photoreduction Coupled with Water Oxidation, *Angew. Chem., Int. Ed.*, 2024, **63**, e202401344.

27 Q. Yao, H. Li, J. Xue, S. Jiang, Q. Zhang and J. Bao, Promoting Photocatalytic H_2 Evolution through Retarded Charge Trapping and Recombination by Continuously Distributed Defects in Methylammonium Lead Iodide Perovskite, *Angew. Chem., Int. Ed.*, 2023, **62**, e202308140.

28 J. T. DuBose and P. V. Kamat, Efficacy of Perovskite Photocatalysis: Challenges to Overcome, *ACS Energy Lett.*, 2022, **7**, 1994–2011.

29 Y. Yang, K. Guo, X. Bai, M. Zhu, S. Wang and S. Liu, Water-stable perovskite nanotube array with enhanced transport of charge carriers induced by functionalized polyoxometalate for the highly efficient photoreduction of uranium(VI), *Inorg. Chem. Front.*, 2025, **12**, 261–272.

30 Z. Zhang, Y. Yang, Y. Wang, L. Yang, Q. Li, L. Chen and D. Xu, Revealing the A–Site Effect of Lead–Free $A_3Sb_2Br_9$

Published on 02 Agda Baxis 2025. Downloaded on 31/05/2026 10:11:58 PM.

Perovskite in Photocatalytic C(sp3)–H Bond Activation, *Angew. Chem., Int. Ed.*, 2020, **59**, 18136–18139.

31 H. Mai, X. Li, J. Lu, X. Wen, T. C. Le, S. P. Russo, D. Chen and R. A. Caruso, Synthesis of Layered Lead-Free Perovskite Nanocrystals with Precise Size and Shape Control and Their Photocatalytic Activity, *J. Am. Chem. Soc.*, 2023, **145**, 17337–17350.

32 K.-K. Guo, Y.-L. Yang, S.-M. Dong, F.-Y. Li, X.-Y. Jiang and L. Xu, Decomposition–Reassembly Synthesis of a Silverton-Type Polyoxometalate 3D Framework: Semiconducting Properties and Photocatalytic Applications, *Inorg. Chem.*, 2022, **61**, 6411–6420.

33 Y. Yang, K. Guo, M. Zhu, A. Zhang, M. Xing, Y. Lu, X. Bai, X. Ji, Y. Hu and S. Liu, Exploring Electron Transfer Mechanism in Synergistic Interactional Reduced Polyoxometalate-Based Cu(I)–Organic Framework for Photocatalytic Removal of U(VI), *Inorg. Chem.*, 2024, **63**, 7876–7885.

34 K.-K. Guo, M. Xu, Y. Zheng, X.-X. Wang, F.-Y. Li, W.-J. Xu and L. Xu, Exploring the Coordination Modes of a Keggin-Type $[ZnW_{12}O_{40}]^{6-}$ Anionic Cluster: Bonding Patterns, Crystal Structure, and Semiconducting Properties, *Inorg. Chem.*, 2021, **60**, 9097–9109.

35 A. Pal, S. Srivastava, P. Saini, S. Raina, P. P. Ingole, R. Gupta and S. Sapra, Probing the Mechanism of Fluorescence Quenching of QDs by Co(III)-Complexes: Size of QD and Nature of the Complex Both Dictate Energy and Electron Transfer Processes, *J. Phys. Chem. C*, 2015, **119**, 22690–22699.

36 H. He, Z. Ye, S. Lin, B. Zhao and J. Huang, Negative Thermal Quenching Behavior and Long Luminescence Lifetime of Surface-State Related Green Emission in ZnO Nanorods, *J. Phys. Chem. C*, 2008, **112**, 14262–14265.

37 C. Li, R. Kang, X. Ma, J. Xie, Y. Wang and T. Seto, Enhanced Quantum Efficiency in $Ca_{2-2x}Na_xGd_xMgWO_6$: Mn^{4+} Phosphors: Allosteric Substitution to Disrupt Local Symmetry for Plant Cultivation Application, *Small*, 2025, 2500640.

38 W. Li, X. Feng, K. Guo, W. Pan, M. Li, L. Liu, J. Song, Y. He and H. Wei, Prominent Free Charges Tunneling Through Organic Interlayer of 2D Perovskites, *Adv. Mater.*, 2023, **35**, 2211808.

39 C. H. Liao, C. H. Chen, J. Bing, C. Bailey, Y. T. Lin, T. M. Pandit, L. Granados, J. Zheng, S. Tang, B. H. Lin, H. W. Yen, D. R. McCamey, B. J. Kennedy, C. C. Chueh and A. W. Y. Ho-Baillie, Inorganic–Cation Pseudohalide 2D $Cs_2Pb(SCN)_2Br_2$ Perovskite Single Crystal, *Adv. Mater.*, 2022, **34**, 2104782.

40 Y. Zhao, Y. Dai, Q. Wang, Y. Dong, T. Song, A. Mudryi, Q. Chen and Y. Li, Anions–Exchange–Induced Efficient Carrier Transport at $CsPbBr_xCl_{3-x}/TiO_2$ Interface for Photocatalytic Activation of $C(sp^3)$–H bond in Toluene Oxidation, *ChemCatChem*, 2021, **13**, 2592–2598.

41 T.-Q. Zeng, B.-H. Wang, S. Tian, Z.-J. Bai, X. Wang, Y. Li, C.-T. Au, L. Chen and S.-F. Yin, Ce Doping Boosts the Photocatalytic Activity of Ultrathin Bi_2MoO_6 Nanosheets for Toluene Selective Oxidation, *Ind. Eng. Chem. Res.*, 2023, **62**, 11573–11584.

 This journal is © the Partner Organisations 2025